Investigation on simultaneous energy harvesting and visible light communication using commercial c-Si PV cells

Bandwidth characterization under colored LEDs

Zhou, Yilong; Ibrahim, Aya; Muttillo, Mirco; Ziar, Hesan; Isabella, Olindo; Manganiello, Patrizio

DOI
10.1016/j.energy.2024.133387

Publication date
2024

Document Version
Final published version

Published in
Energy

Energy 311 (2024) 133387

Contents lists available at ScienceDirect

Energy

journal homepage: www.elsevier.com/locate/energy

Investigation on simultaneous energy harvesting and visible light communication using commercial c-Si PV cells: Bandwidth characterization under colored LEDs

Yilong Zhou *, Aya Ibrahim, Mirco Muttillo, Hesan Ziar, Olindo Isabella, Patrizio Manganiello

Photovoltaic Materials and Devices (PVMD) Group, Delft University of Technology, Mekelweg 4, Delft, 2628CD, South Holland, The Netherlands

ARTICLE INFO

Keywords:
VLC
Solar cells
LED colors
Photovoltatronics

ABSTRACT

Visible light communication (VLC) is a promising complement considering the rising radio frequency spectrum congestion. However, photodiode receivers degrade rapidly under high ambient light (> 200 W/m^2). Photovoltaic (PV) cells, designed for outdoor applications, offer an effective alternative. This work studies the fundamental relationship between various LEDs and seven commercial crystalline silicon (c-Si) PV cell architectures to assess simultaneous energy harvesting and communication. The results reveal that increased PV output inversely affects bandwidth. The impact of PV cell architecture on bandwidth is mainly due to bulk doping concentration and metallization design. Higher doping reduces bandwidth at short circuit but increases it at higher operating voltages. At the transmitter end, higher irradiance levels enhance communication, but this effect is minimal at the PV maximum power point (MPP). Additionally, LED color has a negligible impact on PV cell bandwidth. The highest bandwidth is 215 kHz for Al-BSF(5") under short-circuit, while the lowest is 0.1 kHz for SHJ at MPP. Among the tested c-Si PV architectures, Al-BSF cells exhibit the best communication stability – from 100 kHz to 10 kHz, while SHJ shows the worst – from 100 kHz to 0.1 kHz. TOPCon demonstrates the optimal balance between energy harvesting and communication for Pareto optimality.

1. Introduction

Internet of Things (IoT) connected devices have been seamlessly embedded into our daily lives, facilitated by the rapid development of diverse wireless communication technologies. The connectivity of these devices is dominated by means of wireless fidelity (WiFi), Bluetooth, and cellular networks which predominately communicate information through low radio frequency (RF) spectrum. A recent forecast suggests that the number of IoT-connected devices will double the current count, approaching thirty billion in 2030 [1]. Coupled with the rising user density due to population expansion and urbanization, a shortage in the available RF spectrum for communication is anticipated. Besides the escalating RF communication traffic, the demand for high-speed data transmission is another driving force that motivates researchers to explore higher frequencies for wireless communication. The wider bandwidth inherent in the higher frequency range significantly boosts the transmission data rate. This enhancement is essential for applications like space-to-ground links where a massive amount of data needs to be transmitted within a brief contact window [2]. From the perspective of urban environments, the advancements in autonomous vehicles and smart homes also necessitate high-speed communication to manage the immense data flows among IoT-connected devices in the future smart cities [3].

Although higher frequencies provide a promising avenue for wireless communication, their implementation comes with technical challenges. Electromagnetic waves, by nature, experience energy density reduction as they propagate due to medium-induced attenuation. This effect is more prominent at higher frequencies, resulting in an increased path loss. Using higher frequencies is also more susceptible to obstacles including buildings and foliage in the urban environment, leading to shadow zones where signals are significantly weakened or completely absent [4]. To overcome these challenges, one approach suggests implementing line-of-sight (LoS) paths where the information is beamformed and directed along an unobstructed route between the receiver and transmitter to mitigate attenuation and blockage [5]. Another more widely acknowledged approach involves segmenting the communication into smaller cells so that stronger and more reliable signals are ensured within those confined regions [6]. However, developing such micro-communication units relies on the availability of widespread infrastructures. This requirement has prompted researchers to investigate the potential of visible light communication (VLC) systems that could

* Corresponding author.
E-mail address: Y.Zhou-15@tudelft.nl (Y. Zhou).

https://doi.org/10.1016/j.energy.2024.133387
Received 1 March 2024; Received in revised form 31 August 2024; Accepted 6 October 2024
Available online 11 October 2024

be integrated with existing lighting infrastructure dominated by light-emitting diodes (LEDs), that is, leveraging their extensive deployment. The additional communication channels introduced by the visible light spectrum not only complement the current wireless communication systems, effectively mitigating RF congestion, but also expand the bandwidth, thereby offering high-speed data transmission [7].

Typically, a VLC system consists of a light source (LED or LASER) as the transmitter and photodiodes (PDs) as the receiver [8]. During data transmission, the transmitter intensity is modulated at a high frequency, which in turn modulates the output current of PDs as the light strikes them. This varying current is subsequently translated into voltage signals with a trans-impedance amplifier and decoded to extract the information. The modulation frequency employed is usually much higher than the flicker fusion threshold, meaning that the primary lighting function of the LED infrastructure remains unaffected after integrating with the VLC systems, as the rapid flickering is imperceptible to human eyes [9]. In addition to its wider bandwidth and rapid deployment capabilities, VLC offers a few more advantages over traditional RF communication: firstly, visible light is unlicensed, making it freely available for broad development [10]; secondly, visible light cannot penetrate walls, providing high-security communication by reducing the risks of eavesdropping [11]; lastly, LEDs are energy-efficient, and their long lifespan contributes to a reduced maintenance cost [12]. As a specific application of VLC technology, Light Fidelity (LiFi) facilitates high-speed data transmission by complementing WiFi. The recent introduction of the IEEE 802.11bb standard helps accelerate its adoption, which sets the stage for enhanced interoperability in the wireless communication society [13].

Nevertheless, the extensive implementation of such technology still needs to resolve certain issues, and one of the bottlenecks is found at the receiver end. Despite its fast response time, high sensitivity, and wide bandwidth for optical signals, the frequency response of PDs deteriorates drastically when they are exposed to ambient light higher than 200 W/m^2 [14,15]. This limits its communication performance in well-illuminated indoor environments and restrains its application under outdoor conditions. At the same time, PDs must be reverse-biased to function as light detectors, which necessitates a continuous external power supply.

As an effective solution, PV cells are gaining recognition for self-powered VLC receivers under high ambient light conditions. They are primarily engineered for outdoor operation, and the harvested energy can be utilized to power the entire communication system [16]. One of the first attempts of using commercial silicon PV cells for both communication and energy production was carried out by Kim et al. Their experiment successfully demonstrated VLC operation under strong sunlight irradiance of 800 W/m^2 [17]. Malik et al. developed a mini self-powered VLC system, which offers a bandwidth of 50 kHz and a maximum error-free data rate of 8 kb/s [18]. In a related study, Wang et al. investigated the feasibility of using a PV panel as the detector in an optical wireless communication (OWC) system. They tested both on-off keying (OOK) and orthogonal frequency division multiplexing (OFDM) modulated signals, achieving data transmission rates of 1 Mb/s and 11.84 Mb/s, respectively, while generating 2 mW of electricity [9,19]. By employing a self-reverse-biased circuit to the PV panel, Shin et al. achieved an improved data rate of 17.05 Mb/s [20]. The potential of the underwater OWC system was demonstrated by Kong et al. where they successfully transmitted information from a laser diode through a 7-meter water tank to a solar panel at a rate of 22.56 Mb/s [21]. In 2019, Das et al. built the world's first OWC system using off-the-shelf lasers and silicon PV panel, which harvested 5 W power while communicating at a data rate of 8 Mb/s [22]. The impact of sunlight on PVs as OWC receivers was further explored, and a trade-off between energy harvesting and communication performance was reported. This means that while the PV output increases with solar irradiation, the data rate exhibits a contrary trend, decreasing as the solar irradiation intensifies [23].

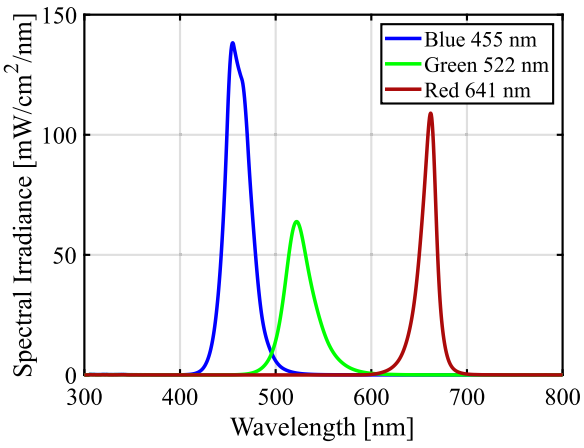

Fig. 1. The measured spectra of blue, green, and red LEDs used in this study. The peak wavelengths are indicated in the legend, and show slight shifts from the values the manufacturer specifies (Blue: 463 nm; Green: 523 nm; Red: 655 nm).

Other research investigated using different PV technologies in VLC systems, where thin film amorphous silicon was demonstrated to support weak light detection (down to 10 mW/m^2), achieving a data rate of 1.2 Mb/s [24]. Organic PV (OPV) is a relatively new field in VLC, but it is gaining interest due to its ease of fabrication and tunable properties [25]. The very first investigation in using OPV as a photodetector was carried out by Arredondo et al. where they demonstrated a bandwidth of 790 kHz based on P3HT:PCBM [26]. Another work done by Vega-Colado et al. realized a full-organic VLC system using off-the-shelf components and achieved a bandwidth of 200 kHz at 2 V of reverse bias [27]. Salamandra et al. developed the inverted P3HT:PCBM organic structure and achieved a bandwidth of 1.02 MHz at −1 V bias [28]. Although various approaches are being explored to improve the bandwidth, reverse biasing the OPV means the device is not generating power. One of the first studies of combining communication and energy harvesting using OPV was conducted by Zhang et al. and they revealed that using an OPV cell as the receiver enabled a data rate of 34.2 Mb/s and concurrently produced a power of 0.43 mW [29]. This outcome has been overtaken by a recent work where a remarkable data rate of 363 Mb/s was reached, with a 10.9 mW power output [30]. Mica et al. used a triple-cation perovskite PV cell as the photodetector and achieved a 56 Mb/s data rate under white LED [31]. One of the best communication performances was reported by employing gallium arsenide (GaAs) PV cells, where a maximum of 1 Gb/s data rate was attained when the PV cell was operating under short-circuit condition [32,33].

While most of the research focuses on enhancing the data transmission speed, the fundamental relationship between the light source and different PV cell architectures is not systematically explored in the context of VLC. Therefore, the aim of this study is to fill this research gap by systematically exploring the communication performance of commercial PV cells with diverse architectures when they are utilized as VLC receivers. Additionally, three representative LED colors within the visible light spectrum are investigated in terms of their impact on the communication performance of commercial PV cells. The objective is to determine if a particular LED color demonstrates superior performance, which could inform future color filter design for PV cells to improve communication. In this work, the frequency response under various light intensities is characterized for each LED color and further conducted at different PV cell operating voltages to understand the dynamics between energy harvesting and data communication. c-Si PV cells are the primary focus due to their dominating position in the PV industry. These include architectures such as 5-inch aluminum back surface field (Al-BSF(5″)), 6-inch Al-BSF (Al-BSF(6″)), busbar-free Al-BSF (Al-BSF(BF)), passivated emitter rear contact (PERC), interdigitated

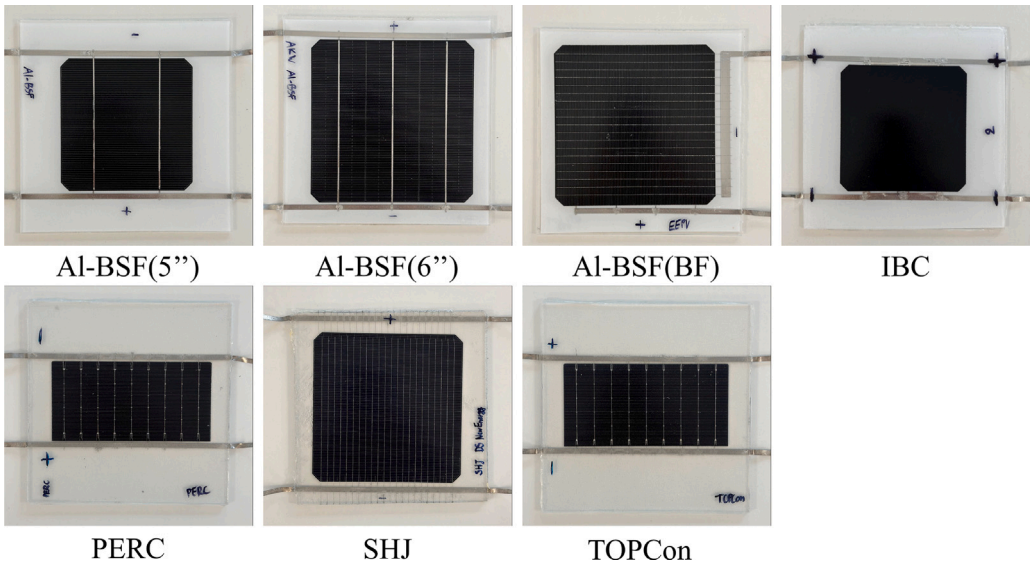

Fig. 2. Photos of the commercial PV laminates used in this study.

back contact (IBC), silicon heterojunction (SHJ), and tunnel oxide passivated contact (TOPCon), covering from the oldest to the newest c-Si PV technologies. It is worth mentioning that all the commercial PV cells are maintained in their original dimension for this study. Certainly, cell size plays a role in determining the capacitance and resistance of PV cells, where a larger cell size generally leads to higher capacitance and lower resistance [34]. But these parameters are also highly dependent on other factors, including the bulk doping concentration, emitter resistance, and the design of fingers and busbars [35]. This detailed architectural information of commercial solar cells is not readily available and cannot be easily extracted from measurements. Additionally, standardizing the cell size would require cutting all the commercial solar cells down to half-size, potentially introducing unexpected edge effects and leading to performance deviations [36]. To maintain the integrity of our study, we retained the original dimensions of all PV cells. This approach allows us to evaluate the energy harvesting and communication performance of off-the-shelf PV cells within the context of VLC without introducing unwanted performance degradation due to cell cutting. Keeping the cells in their original size also ensures that our results are directly applicable to consumer-grade products, providing valuable insights for both researchers and industry professionals.

The rest of the paper is structured as follows: in Section 2, the experimental setup is introduced, including the setup for I–V curve measurement and bandwidth characterization; Section 3 elaborates the methods for measurement data processing; Section 4 presents and discusses the measurement results, analyzing the relationship between bandwidth and PV operating voltages, LED intensities, LED colors, and PV cell architectures; finally, the conclusions are drawn in Section 5.

2. Experimental setup

The PV cells are first laminated (hereafter referred to as PV laminates), and the lamination structure comprises a stratified assembly including, from top to bottom, a PV glass layer, an ethylene vinyl acetate (EVA) encapsulant layer, the PV cell, another EVA layer, and a white back sheet or a PV glass layer. These PV laminates are examined under three representative LED colors across the visible light spectrum, spanning from red to green and blue, with a maximum rated power of 100 W. The spectral distributions of the LEDs are measured with a spectrometer (SR-1901PT) and are presented in Fig. 1, with their peak wavelength indicated in the legend [37]. The photos of the tested commercial PV laminates are shown in Fig. 2, and their architectural information is detailed in Table 1. The characteristics of PV laminates under standard test conditions (air mass 1.5 spectrum, 1000 W/m^2 of irradiance, and cell temperature of 25 °C) are listed in Table 2. For each LED color, the PV laminates are tested at three irradiance levels: 100, 300, and 500 W/m^2. As the output current of solar cells is proportional to the incident light intensity, increasing the LED intensity will generate more current that flows through the system and brings up the temperature. The attached heat sink has a limited capacity to dissipate only a certain amount of heat. This limits the maximum LED intensity used in the measurement to prevent the components from overheating damage. Therefore, the maximum irradiance intensity is determined based on the heat dissipation capacity of the system's heat sink.

Fig. 3 presents the experimental setup for the measurements. The measurement process can be divided into two primary stages. For each LED color and intensity setting, the I–V behavior of PV laminates is first characterized to identify their open-circuit voltage and maximum power point. Following this initial characterization, the PV laminates are biased at various operating voltages to perform the small-signal bandwidth measurement. The selection of operating voltage ranges and increments is guided by the outcomes of the I–V characterization. The measurement details of these two stages are elaborated in the subsequent two subsections.

2.1. I-V curve measurement of PV laminates

The I–V curves of PV laminates are measured in a 4-wire configuration with Keithley KickStart software and source meter (Keithley 2651A). A simplified diagram of this setup is depicted in Fig. 4a. The light source consists of a matrix of LEDs. During the measurement, it is fitted with a collimator lens and placed 10 cm above the PV laminates to ensure a comprehensive and homogeneous illumination. By adjusting the output power of the LED, the targeted irradiance level is achieved, as indicated by the short-circuit current of PV laminates. This is due to the linear correlation between the incident light intensity and the short-circuit current produced by the PV laminates. The temperature of PV laminates is monitored with a Pico logger connected to a thermocouple attached to the rear side of the PV laminates. Once the temperature stabilizes, the I–V sweep is performed. The resultant I–V curve is plotted in Fig. 4b in blue, which represents the case for IBC PV laminate under

Table 1
Architectural information of the c-Si PV laminates, with abbreviations: BB for busbar, SW for smart wire, and BC for back contact. The bulk doping concentration of tested commercial c-Si solar cells was determined by using C-V measurement [38].

PV laminate [–]	Cell size [–]	Area [cm^2]	Doping concentration [$atoms/cm^3$]	Front-side metal [–]	Back-side metal [–]
Al-BSF(5″)	Full-size	153.0	4.2×10^{14}	2BB	2BB
Al-BSF(6″)	Full-size	244.3	1.1×10^{16}	3BB	3BB
Al-BSF(BF)	Full-size	244.3	1.0×10^{16}	19SW	4BB
IBC	Full-size	153.0	4.5×10^{14}	–	BC
PERC	Half-cut	126.0	2.6×10^{16}	9BB	9BB
SHJ	Full-size	244.3	5.6×10^{15}	22SW	22SW
TOPCon	Half-cut	126.0	4.5×10^{15}	9BB	9BB

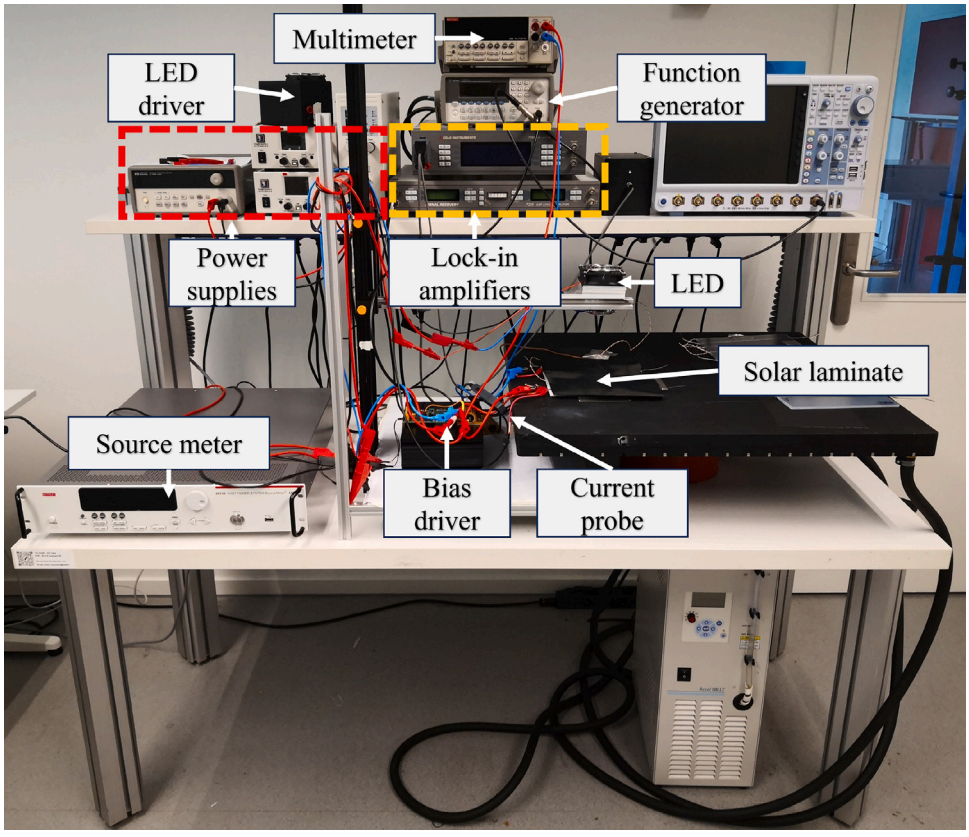

Fig. 3. Experimental setup for I–V curve characterization and bandwidth measurement.

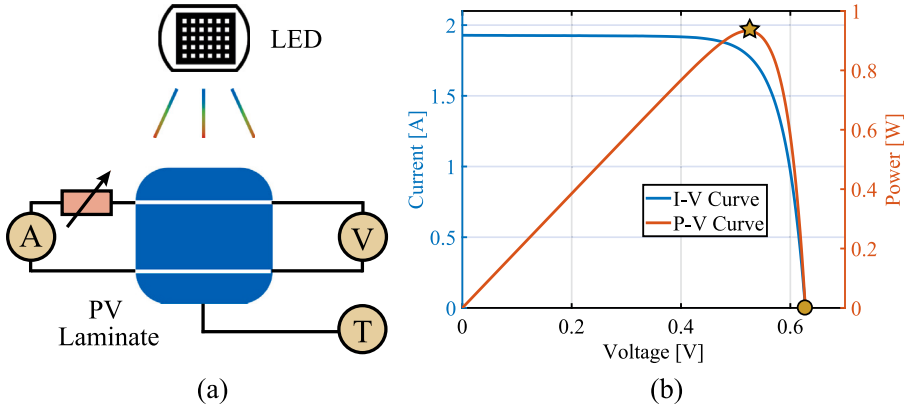

Fig. 4. (a) Diagram of the I–V characterization setup where the PV laminate is measured with a 4-wire configuration under different LED colors and intensities. The temperature of the PV laminate is monitored with a thermocouple attached to the back of the laminate, and all I–V sweeps are conducted after the temperature is stabilized; (b) I–V and P–V characteristics of the IBC PV laminate under blue LED at 300 W/m^2 and 30 °C. Both the maximum power point and the open-circuit voltage are highlighted in the plot.

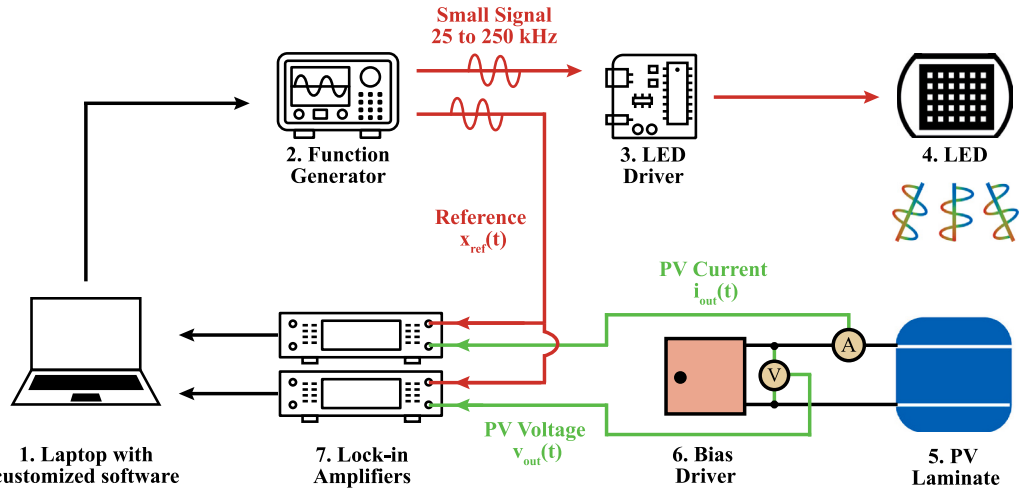

Fig. 5. Bandwidth characterization setup for the VLC system when c-Si PV laminates are used as the receiver. The bias circuit is developed to set the operating voltage of PV laminates and it imposes a resistive load R_f in the AC circuit system.

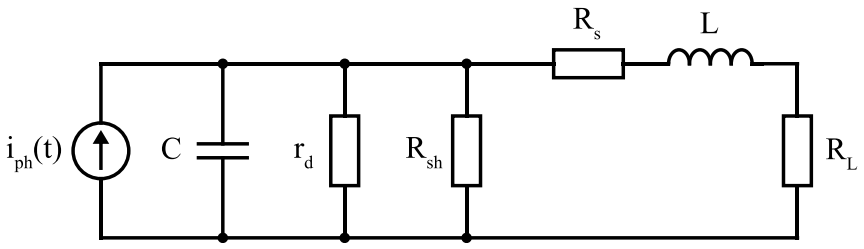

Fig. 6. The small-signal AC equivalent circuit of a PV laminate connected to a load resistance under illumination [41].

Table 2
Key parameters of the c-Si PV laminates under standard test conditions (STC) obtained using a LOANA solar cell analysis system [39].

PV laminate [–]	V_{oc} [V]	I_{sc} [A]	V_{mpp} [V]	I_{mpp} [A]	P_{mpp} [W]
Al-BSF(5″)	0.64	5.96	0.51	5.51	2.79
Al-BSF(6″)	0.64	9.44	0.52	8.91	4.65
Al-BSF(BF)	0.64	9.44	0.51	8.86	4.48
IBC	0.68	6.46	0.56	5.98	3.39
PERC	0.69	4.94	0.59	4.71	2.76
SHJ	0.74	8.92	0.64	8.50	5.40
TOPCon	0.69	4.91	0.59	4.65	2.74

blue LED at 300 W/m^2 and 30 °C. As the voltage increases, it can be observed that the current decreases. The voltage at which the output current of PV laminate is zero is known as the open-circuit voltage (V_{oc}). Additionally, the power output of PV laminate as a function of the operating voltage is also depicted by the red curve in Fig. 4b, where the power output first increases with the voltage to a peak, then it declines to zero. This peak represents the maximum power point (MPP), and it is the optimal operating point when PV laminate is used as an energy harvester. Measuring the I–V curve is an important step because it not only characterizes the electrical properties of PV laminate but the obtained V_{oc} and MPP are also essential to determine the operating voltage range for the subsequent small-signal frequency sweep. It is worth mentioning that the temperature effect is not considered in the analysis due to the absence of temperature control components in the setup. An increased temperature alters the I–V curve, leading to higher short-circuit current and lower open-circuit voltage, eventually reducing the solar cell's power output [40].

2.2. Bandwidth measurement of PV laminates

Fig. 5 shows the diagram of the bandwidth characterization setup for the VLC system using c-Si PV laminates as the receiver. The transmitter circuit consists of a function generator (Agilent 33250A), a custom-made LED driver, and LEDs with a collimator lens. The receiver circuit comprises PV laminates, a self-made bias driver, a multimeter (Keithley 2000), and two lock-in amplifiers (EG&G 7260 and EG&G 7225). Both circuits are connected to a single laptop, which controls and processes the signals using in-house developed measurement software. It should be noted that all these setup components have relatively high bandwidth, thus, their contribution to the bandwidth measurement of PV laminates is negligible.

2.2.1. The transmitter circuit

The transmitter circuit essentially controls the operation of the LED light source. The laptop sends the control signals, encompassing both DC and AC components, to the function generator. The function generator then relays the requisite composite waveform to the LED driver, which modulates the LED to operate in the desired manner. In this setup, the LED operates in a constant current (CC) mode, which is a preferred approach for driving high-power LEDs to prevent thermal runaway risks. By maintaining a constant current, the CC mode also helps ensure a stable light output and reduce chromaticity shift [42]. As mentioned in Section 2.1, the DC component is set according to the short-circuit current of PV laminates that changes linearly with the incident irradiance level. Superimposed on this DC baseline is a small sinusoidal AC signal with a peak-to-peak amplitude (V_{pp}) of 5 mV, resulting in a light intensity change of around 1 W/m^2. The frequency variation ranges from 25 to 250 kHz, where the maximum frequency of this range is determined by the input frequency limit of the lock-in amplifier. It is worth mentioning that in the current setup, LEDs serve a dual role as both a light source and a transmitter. In practical scenarios,

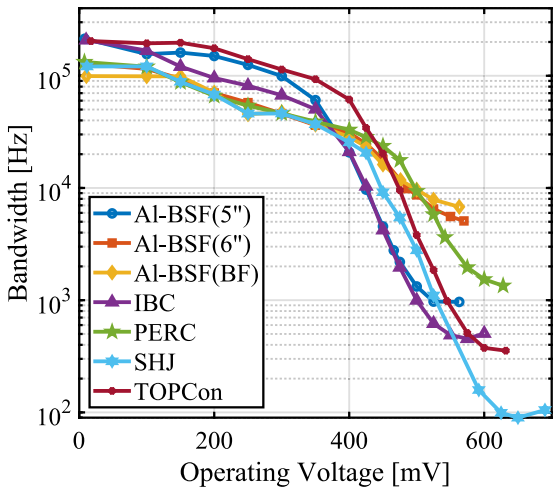

Fig. 7. Voltage bandwidths of PV laminates with respect to the operating voltages under blue LED at 100 W/m^2.

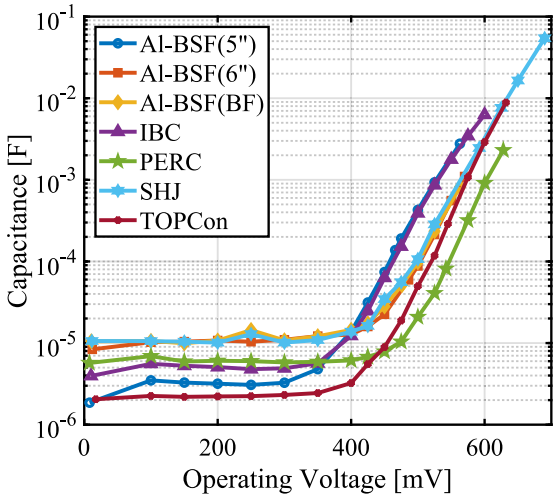

Fig. 8. Capacitance of PV laminates with respect to the operating voltages under blue LED at 100 W/m^2.

the solar cells are exposed to ambient light for electricity generation. Particularly in outdoor applications, the PV modules are subject to the solar spectrum, which can introduce unexpected noises during data transmission. In future iterations of the setup, a solar simulator can be incorporated to provide the PV laminates with consistent exposure to a solar spectrum, while LEDs are exclusively used for data transmission.

2.2.2. The receiver circuit

The receiver circuit essentially extracts the frequency response signal from the PV laminate outputs. This dynamic behavior of PV laminates is modeled with a small-signal AC equivalent circuit, as shown in Fig. 6, with a current source representing the dynamic photo-generated current i_{ph} at a certain time instance. The diode component in the DC equivalent circuit of solar cells is translated into a combination of capacitor and dynamic resistor, allowing for a detailed analysis of the dynamic behavior of solar cells under small-signal AC conditions. Besides the series resistance R_s and shunt resistance R_{sh} of the PV laminates, an additional voltage-dependent internal dynamic resistance r_d is included. The capacitance effect of the PV laminate is modeled with a capacitor C, and the inductor L represents the inductance due to the PV cell's metalization and its interconnection with the load resistance R_L.

During the frequency sweep, the bias driver first sets the operating voltage of the PV laminates to simulate various levels of power output. The range for adjusting the operating points is determined from the previous step of I–V measurement, and both the operating voltage and illumination level are fixed at each frequency sweep, meaning that the bandwidth is characterized after the PV laminate has reached charge distribution equilibrium [43,44]. At each operating voltage, the frequency sweep is performed where the modulated LED illuminates the PV laminate. In response to the varying light intensity, the PV laminate shifts its I–V characteristics accordingly. These shifts are relatively subtle, as the amplitude of the AC signal is very small compared to the DC baseline. Such tiny variations in the PV output are buried in the system noises, therefore, lock-in amplifiers are employed to extract this small-signal AC information. In this setup, both the AC PV voltage and current outputs are measured. The AC PV voltage is directly read with a voltage probe connected to one of the lock-in amplifiers, while the AC PV current is first converted using a current probe (YOKOGAWA DLM5038) before being fed into the other lock-in amplifier. For both lock-in amplifiers, the peak-to-peak signal at low frequency (25 Hz) is adopted as the reference signal (X_{ref}), and the signal gain at various modulation frequencies f is calculated by the following equation:

$$Gain(f) = 20log_{10}\frac{X_{out}(f)}{X_{ref}} \tag{1}$$

where $X_{out}(f)$ is the peak-to-peak voltage or current signal at each frequency under a specific operating point. Since PV laminates act as low-pass filters for the received small light signals, the frequency at −3 db gain (also known as the cut-off frequency f_c) with respect to the global peak is the bandwidth [38]. This measurement enables the determination of bandwidth for all the PV laminates, which are biased at different operating points and subject to various LED colors and intensities.

3. Methodology

To evaluate the bandwidth accurately, it is important to process and compensate the measurement data. This adjustment addresses two primary sources of deviation in the results: the ballast resistance found in the bias driver and the inductance in the system that causes resonance.

3.1. Offset the ballast resistance in bias driver

The bias driver acts as a resistive load to configure the operating point of the PV laminate as introduced in Section 2.2.2. However, this bias driver does not perform as an ideal variable resistor due to the presence of a fixed one-ohm ballast resistance R_f in series. While this ballast resistance is essential to stabilize the PV output signal, enabling a successful measurement, it also deviates the measured bandwidth from the true values. For a clearer understanding, the bandwidth f_c of an RC low-pass filter tailored for this specific scenario is shown in the equations below:

$$f_c = \frac{1}{2\pi RC} \tag{2}$$

where

$$R = (r_d \parallel R_{sh}) \parallel (R_s + R_L + R_f) \tag{3}$$

When the PV laminate operates at high voltages, the load resistance R_L dominates the bias driver resistance, meaning that the impact of R_f on the measured bandwidth is negligible. In contrast, at low operating voltages, R_f is comparable with R_L. Thus, its impact on the measured bandwidth becomes significant, which leads to a reduced bandwidth according to Eq. (2). To offset the effect of the additional ballast resistance, the measured bandwidth needs to be compensated

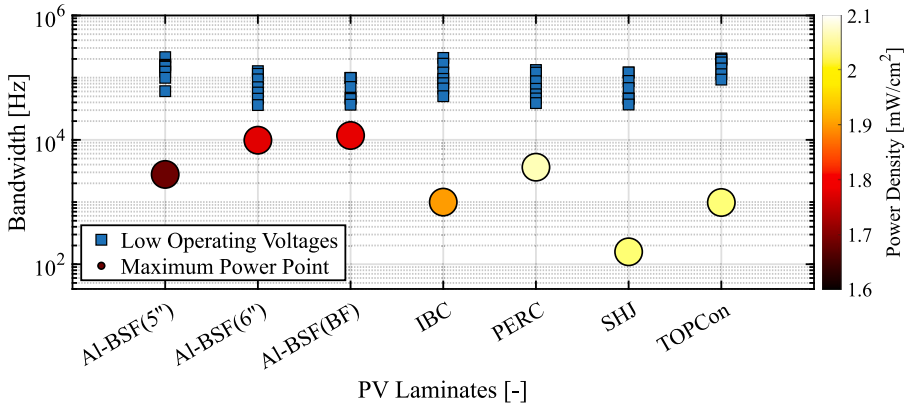

Fig. 9. Voltage bandwidths of PV laminates obtained at low operating voltages and maximum power points under blue LED at 100 W/m^2, represented by blue squares and colored circles, respectively. The circle color indicates the magnitude of the power density the PV laminate delivers at the maximum power point.

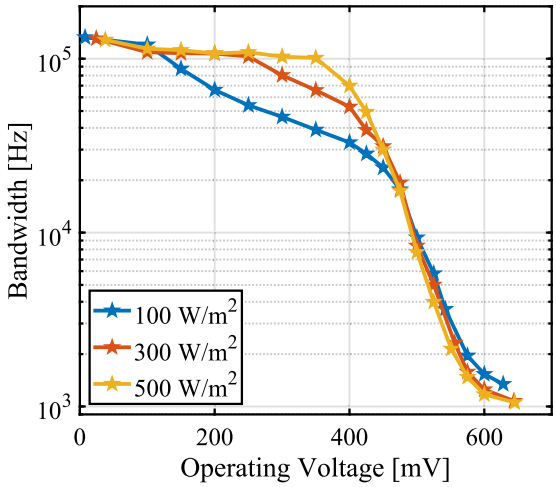

Fig. 10. Voltage bandwidths of PERC laminate with respect to the operating voltages, measured under blue LED at 100, 300, and 500 W/m^2.

by considering the resistance R' that excludes the contribution of R_f. The corrected bandwidth, denoted as f_c', is calculated by the following equation:

$$f_c' = \frac{1}{2\pi R' C} \tag{4}$$

Assuming the capacitance C remains unchanged, this expression can be refined by substituting Eq. (2) and becomes:

$$f_c' = \frac{R}{R'} f_c \tag{5}$$

where

$$R' = (r_d \parallel R_{sh}) \parallel (R_s + R_L) \tag{6}$$

R_s is the series resistance of PV laminates extracted by fitting the measured I–V curve with the double-diode model of PV cells [45]. R_L is the imposed load resistance depending on the operating point. $(r_d \parallel R_{sh})$ can be obtained from the external dynamic resistance R_D [46]:

$$R_L = V_{op}/I_{op} \tag{7}$$

$$R_D = \Delta V/\Delta I = (r_d \parallel R_{sh}) + R_s \tag{8}$$

where V_{op} and I_{op} are the voltage and current of the PV laminate at the operating point. $\Delta V/\Delta I$ is the inverse of the slope of the measured I–V curve at the given operating point.

3.2. Include the inductance-induced resonance

The bandwidth obtained by removing the ballast resistance does not account for the effect of inductance. This inductance mainly comes from the metallization and interconnections of PV laminates, with the former playing a dominant role. Its presence can make the system oscillate, and the frequency at which this oscillation happens is the resonant frequency, which can be calculated by the following equation:

$$f_r = \frac{1}{2\pi\sqrt{LC}} \tag{9}$$

Given that the bandwidth is the first frequency at which the gain drops below −3 dB, it is important to identify whether this reduction is attributed to the resonant frequency or the cut-off frequency that occurs first. Failure to identify the actual scenario could lead to an overestimation of the system bandwidth, especially at low PV operating voltages where the influence of inductance is significant. Under such conditions, the system bandwidth could be dictated by the resonant frequency, which typically falls below the corresponding RC circuit cut-off frequency. To adjust for this and determine the bandwidth accurately, the correction after considering the inductance-induced resonance is mainly performed by comparing the bandwidths derived from Eq. (4) for the cut-off frequency and Eq. (9) for the resonant frequency, where the lower of these two values is selected as the true bandwidth of the PV laminate. This condition can be exclusively expressed in terms of the damping ratio:

$$\zeta < \frac{1}{2} \tag{10}$$

Upon determining the inductance, the damping ratio is examined for each frequency sweep measurement result, and the bandwidth is corrected for the instances that satisfy the condition. Here, the inductance is considered as independent of the operating voltages, as the change caused by which is negligible [38]. For more information regarding the determination of the damping ratio condition and the inductance, please refer to Appendix.

4. Results and discussion

In this section, the bandwidths of PV laminates under different measurement conditions are presented, focusing on the interplay between two key parameters of the PV laminates: the operating voltage, indicative of the energy harvesting ability, and the bandwidth, which reflects the communication performance. The bandwidth can be measured for both PV current and PV voltage. Here, the voltage bandwidth is primarily explored due to two considerations: first, the voltage bandwidth mirrors the behavior of the current bandwidth, showing close bandwidth results across the measurements; second, using voltage modulation is aligned with practical application, bypassing the additional conversion step from current to voltage [47].

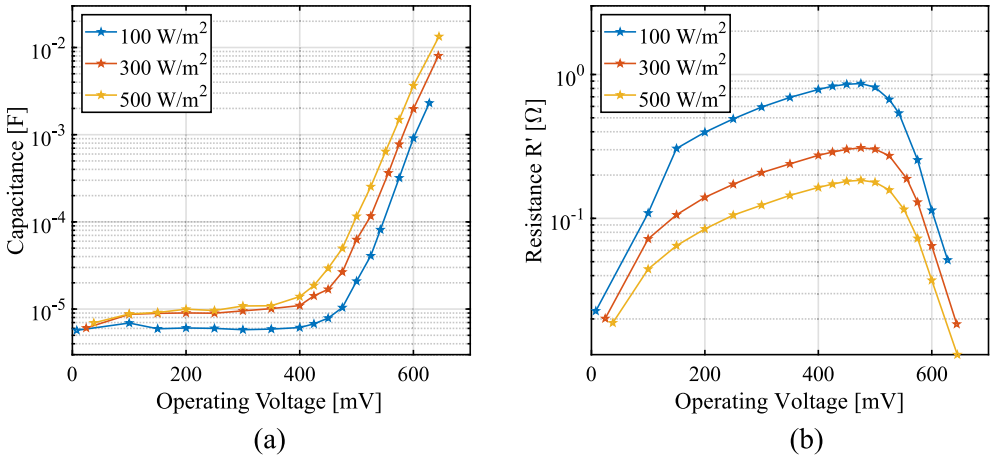

Fig. 11. (a) The capacitance of PERC laminate changing with the operating voltage under blue LED at 100, 300, and 500 W/m^2; (b) The resistance R' of PERC laminate changing with the operating voltage under blue LED at 100, 300, and 500 W/m^2.

4.1. Bandwidth vs. PV operating voltages

Fig. 7 shows the voltage bandwidths of PV laminates with respect to various operating voltages (from short-circuit to open-circuit) under blue LED at 100 W/m^2. As the operating voltage increases, a consistent decrease in the bandwidth is observed across all PV laminates, and two distinct variation regions are identified. In the low operating voltage range (<350 mV), the bandwidth declines gently with increasing operating voltages, while it ramps down exponentially in the high operating voltage range. Such behavior is observed under all measurement conditions, and it can be primarily attributed to the change in the internal capacitance of PV laminates. Fig. 8 illustrates the change of PV capacitance in response to the operating voltage increase. It is evident that in the low operating voltage range, the PV capacitance exhibits minimal change, indicating a dominant influence of depletion capacitance. As the operating voltage continues to increase, the diffusion capacitance becomes the primary driver and determines the exponential increase of the overall capacitance of PV laminates [38,43]. This result indicates that the higher PV output power is achieved at the expense of communication bandwidth. Therefore, a trade-off exists between energy harvesting and communication when PV cells are used as VLC receivers.

Fig. 9 shows a comparative summary of the voltage bandwidths of the individual PV laminates. This comparison includes the bandwidths obtained at the low operating voltage range (marked by blue squares) and at the maximum power point (indicated by colored circles). Additionally, the power density that PV laminates deliver at maximum power point is represented through a color scale with a corresponding color bar. It can be observed that all PV laminates exhibit a notably higher bandwidth at low operating voltages, with their values falling within a comparable range (30 kHz to 200 kHz). Particularly, Al-BSF(5″), IBC, and TOPCon PV laminates present slightly higher overall bandwidth, meaning that they are more advantageous in communication when working at low operating voltages. In contrast, when the PV laminates are optimized for energy harvesting, the bandwidths at the maximum power point scatter across a broad spectrum. Specifically, Al-BSF(6″) and Al-BSF(BF) laminates demonstrate the highest bandwidths (9.8 kHz and 11.7 kHz, respectively) but are subject to lower power output. Conversely, with a higher power density, the SHJ PV laminate shows the least favorable communication performance, with the bandwidth limited to only 0.2 kHz. The PERC laminate outperforms others in power generation while maintaining a reasonable communication bandwidth. Meanwhile, it can also be concluded that the bandwidth variation range of both Al-BSF(6″) and Al-BSF(BF) laminates is narrower than that of others in response to the operating voltage increase. This suggests that they can achieve higher output power with less compromise in communication performance. The underlying cause of this behavior can be attributed to the differences in cell architecture and material properties, such as wafer dopant concentration, which dictate the dynamic response of PV laminates [38].

4.2. Bandwidth vs. irradiance levels

Fig. 10 shows the voltage bandwidth of PERC laminate as a function of the operating voltages under blue LED at 100, 300, and 500 W/m^2. A distinct operating voltage window with a notable bandwidth difference can be identified where the PERC laminate exhibits higher bandwidths under higher irradiance levels. Beyond this specified window, the bandwidths present a marginal difference. This pattern appears to be minimally influenced by the capacitance, as depicted in Fig. 11a, where the laminate capacitance shows only a slightly higher response under higher irradiance levels. The primary determining factor can be attributed to the larger resistance R' of the laminate under low light conditions [48]. As demonstrated in Fig. 11b, the resistance under low irradiance levels remains constantly higher across the entire operating voltage range, and its impact on the bandwidth is more pronounced at low operating voltages where depletion capacitance dominates over diffusion capacitance. Meanwhile, the increased resistance under low-light conditions leads to an overdamped system, resulting in a bandwidth decline at lower operating voltages. For instance, the bandwidth of PERC laminate begins to decrease at 150 mV under 100 W/m^2, in contrast to 300 mV under 300 W/m^2. Therefore, it can be concluded that the irradiance level has minimal impact on the communication performance when the solar laminate is working at the maximum power point for optimized energy harvesting, but a higher irradiance level is preferred when the solar laminate is operating at voltages below the MPP yet distant from the short-circuit condition due to better communication performance. Fig. 12 presents the voltage bandwidth of the remaining PV laminates changing with the operating voltages under different irradiance levels, and a similar trend is observed. It is worth noting that Al-BSF(6″), Al-BSF(BF), and SHJ PV laminates are only measured up to 300 W/m^2 due to the heat dissipation capacity of the bias driver. Similar conclusions can be drawn for other LED colors under the same measurement conditions, suggesting that the impact of light intensity on the communication performance of solar laminates under test is independent of the LED colors.

4.3. Bandwidth vs. LED colors

In fact, the effect of LED color on the communication performance of PV laminates is found to be minimal, as depicted in Fig. 13 where

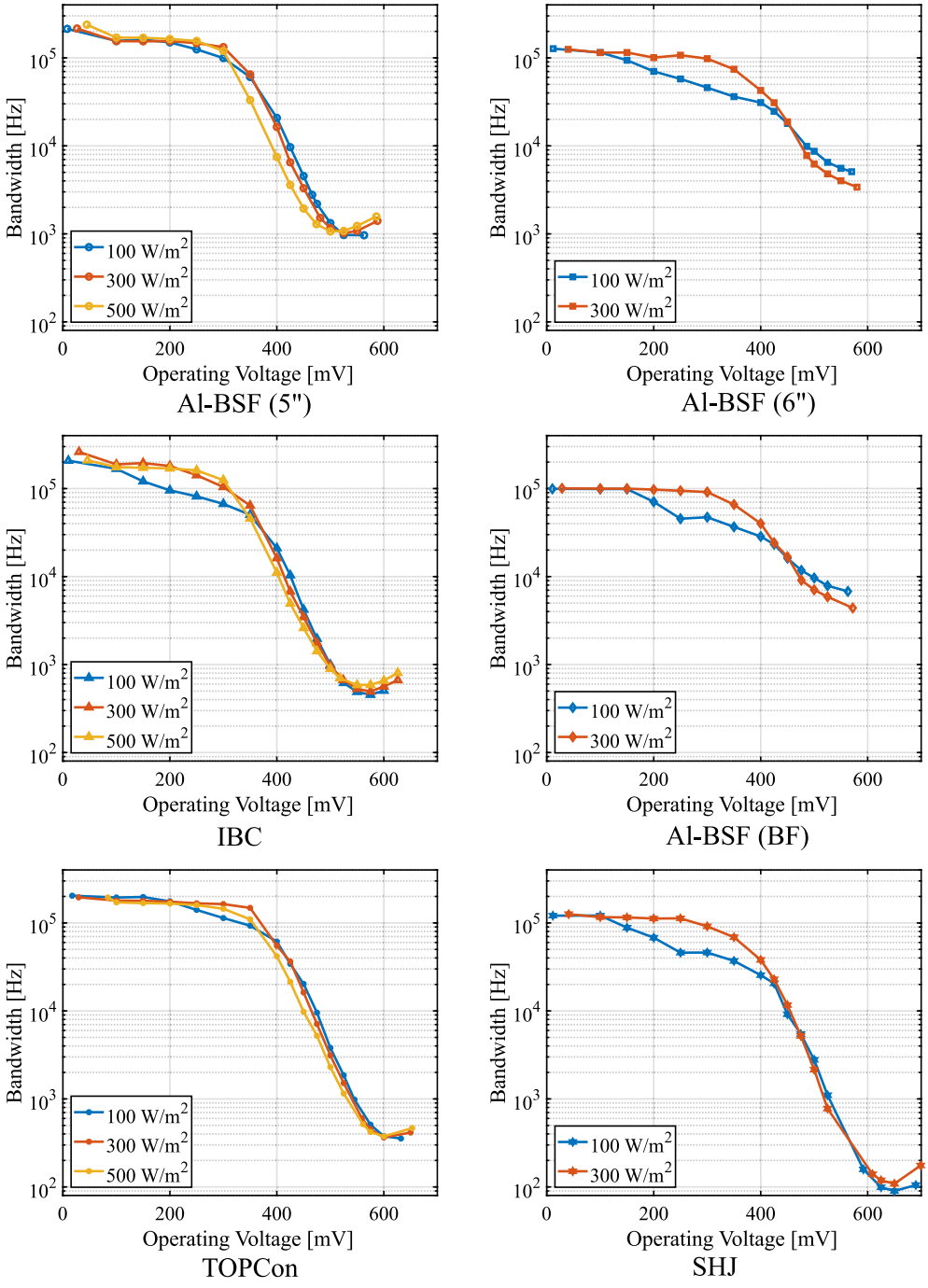

Fig. 12. Voltage bandwidth of the remaining PV laminates as a function of operating voltage under blue LED at 100, 300, and 500 W/m^2.

the voltage bandwidth of PERC laminate presents a consistent response across the entire operating voltage range under blue, green, and red LEDs configured at 100 and 300 W/m^2. Although the blue LED marginally outperforms the red LED in the low operating voltage range under 100 W/m^2 illumination, the variance is relatively minor. At the maximum power point, the bandwidths are nearly the same with negligible difference. Moreover, as the irradiance level increases, the difference in bandwidth becomes even more insignificant. This trend is consistently observed for all the other PV laminates, as shown in Fig. 14. Therefore, from the receiver's perspective, the color of the light source appears to have a limited impact on the communication performance. This uniformity can be advantageous to the integration of wavelength division multiplexing (WDM) with LEDs, ensuring that none of the channels will become a bottleneck. The consistent bandwidth performance across the RGB colors also simplifies the color filter design when multiple PV cells are used for signal separation and demodulation [49]. However, when considering the efficiency of LEDs, using blue LEDs is found to be more advantageous due to their higher energy efficiency [50]. In other words, blue LEDs in a PV-based VLC system would consume less energy than red LEDs to achieve comparable levels of communication performance and energy harvesting. Red LED, by contrast, is preferred in the system where relatively long-distance communication is required due to less atmospheric attenuation while traveling [51].

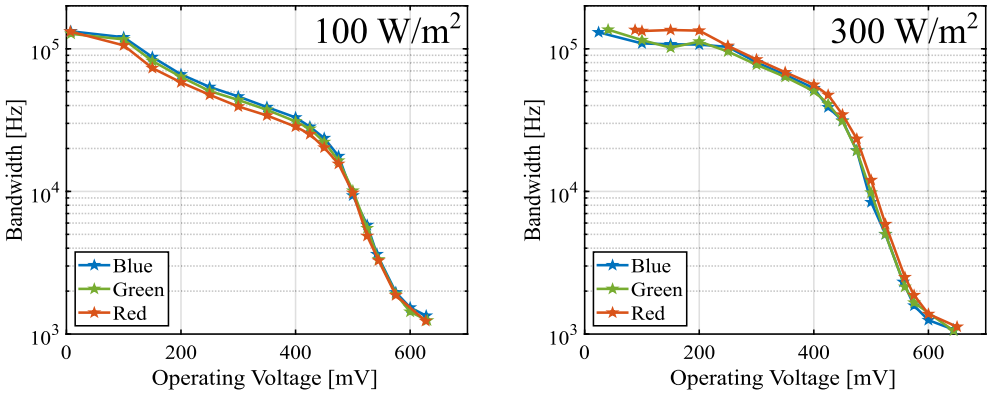

Fig. 13. Voltage bandwidth of PERC PV laminate under blue, green, and red LEDs at 100 and 300 W/m^2.

4.4. Bandwidth vs. architecture of commercial c-Si PV cells

The architectural impact of PV cells on bandwidth can be investigated through the bulk doping concentration and the metallization design. These properties are crucial in determining the capacitance and resistance of tested PV cells, particularly given that their available information is limited. Fig. 15 shows the voltage bandwidth of PV laminates at both the short-circuit condition and the maximum power point under blue LED at 300 W/m^2. The PV laminates along the X axis are reorganized to incorporate the magnitude of doping concentration, where from left to right, it increases from the lowest (Al-BSF(5″)) to the highest (PERC). Under the short-circuit condition (indicated by blue circles), higher doping concentrations tend to result in lower bandwidths. This effect is primarily attributed to the increased depletion capacitance associated with heavier doping profiles. Notably, two outliers are observed, where PV laminates IBC and Al-BSF(BF) exhibit significantly higher or lower bandwidths compared to adjacent cases. This behavior can result from the difference in series resistance as shown in Fig. 16. With nearly identical doping concentrations, the series resistance of IBC laminate is half that of the Al-BSF(5″) laminate owing to its optimized metallization layout, which leads to a higher bandwidth. Although the series resistance of TOPCon is even lower than that of IBC laminate, its doping concentration is one order of magnitude higher than that of the latter, resulting in a higher depletion capacitance and thereby bringing down the bandwidth. This mechanism also applies to SHJ, Al-BSF(BF), and Al-BSF(6″) PV laminates. Therefore, for VLC applications under short-circuit conditions, it is preferred to use PV laminates with lower doping concentration and lower series resistance achieved from an optimal metallization design.

The bandwidths at the MPP of each PV laminate (indicated by red hexagrams) do not show a clear trend as the doping concentration increases. This variability happens because the PV laminates are biased at their own MPP voltage, which differs from cell to cell. These varying voltages can significantly alter the diffusion capacitance and overall resistance, leading to irregular bandwidth results observed in Fig. 15. To provide a more insightful comparison among PV laminates, Fig. 17 plots the bandwidths of PV laminates with each color bar representing the bandwidths at operating voltages from 450 to 550 mV displayed from top to bottom. The bandwidths at 475 mV are connected by a black line. Unlike the results at MPP, the bandwidths of PV laminates under the same bias voltages present a more obvious pattern. Within the high operating voltage range, the bandwidth tends to be higher for the PV laminates with higher doping concentrations. This effect is mainly due to the lower diffusion capacitance of the PV laminates with higher doping concentrations. Opposite to the short-circuit conditions where higher doping concentration results in increased depletion capacitance, the diffusion capacitance under high operating voltage range is reversely associated with the doping concentration; in other words, higher doping concentration leads to lower diffusion capacitance [38]. Notably, TOPCon PV laminate shows higher bandwidth because its series resistance is much lower than that of SHJ despite having a close doping concentration. Therefore, for VLC applications around MPP, it is preferable to use PV laminates with high doping concentration and low series resistance.

Based on the above observations, optimizing the metallization design for a lower series resistance is clearly beneficial for both energy harvesting and communication. Since PV cells typically operate at MPP to maximize their energy production, increasing the doping concentration is advantageous to achieve a higher bandwidth around MPP, provided it does not adversely affect the conversion efficiency of PV cells. In theory, PV modules composed of these PV cells should maintain the same bandwidth because connecting the cells in series proportionally reduces the overall capacitance and increases the overall resistance, which effectively cancels out their individual impact on the bandwidth. However, the additional metallization required for the cell interconnection and the junction box can introduce extra resistance to the system, which could eventually lead to a lower bandwidth at the module level.

4.5. Trade-off between energy harvesting and communication

To get a better insight into the trade-off between energy harvesting and communication in a PV-based VLC system, Fig. 18 illustrates the relationship between the bandwidth of PV laminates and their power output under the given illumination conditions. This reaffirms that the improvement in communication performance often comes at the expense of reduced power output. Notably, the bandwidth response of Al-BSF(6″) and Al-BSF(BF) PV laminates is more resilient to the increase in output power, implying that achieving comparable increases in the ratio of output power requires relatively smaller sacrifice in the bandwidth. In contrast, the SHJ PV laminate exhibits the least favorable bandwidth response against the output power. As compared in Fig. 19, the SHJ PV laminate experiences a significant power decrease to achieve a bandwidth of 70 kHz, losing 40% of its maximum power output. Meanwhile, Al-BSF(5″) and Al-BSF(BF) PV laminates are able to retain nearly 80% of their maximum power output when operating under similar bandwidth. This makes them the most suitable c-Si PV cell architecture in the VLC system in terms of individual trade-off between energy harvesting and communication, that is, when the system is optimized for its overall communication stability.

Given the tradeoff between energy harvesting and communication, that is, maximizing energy harvesting comes at the expense of communication performance and vice versa, the Pareto optimality emerges as a compelling indicator to assess the overall performance of PV-based VLC systems [52]. This concept provides valuable insights into the solution that represents the best possible compromise between conflicting objectives, where in the context of a PV-based VLC system,

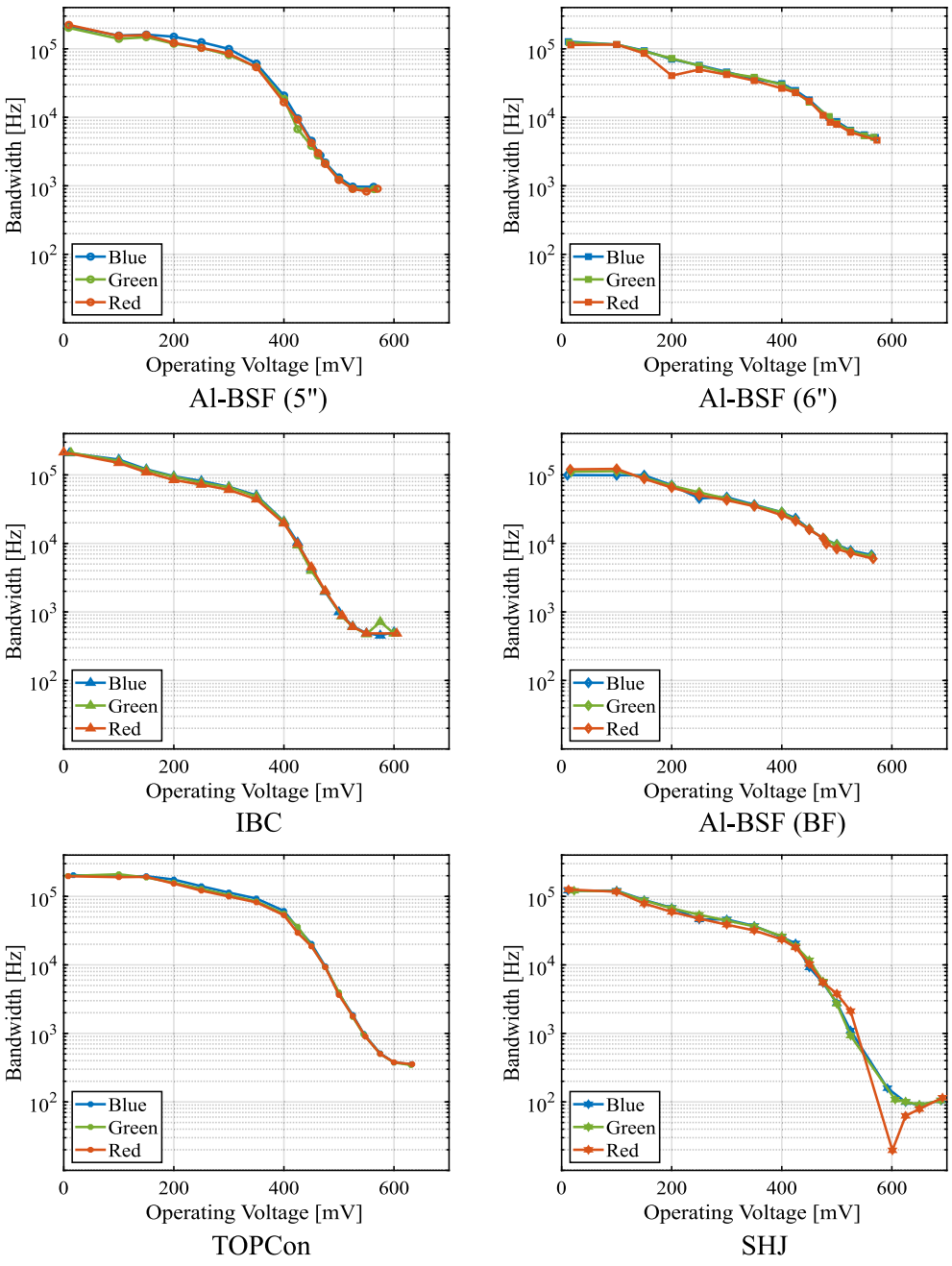

Fig. 14. Voltage bandwidths of the remaining PV laminates as a function of the operating voltage under blue, green, and red LEDs at 100 W/m^2. The outlier in SHJ PV laminate at 600 mV could result from measurement error.

Table 3
Bandwidth and power density of all PV laminates at Pareto optimality, along with their normalized power density (nPD) and normalized bandwidth (nB).

PV laminate [–]	Bandwidth [kHz]	Power density [mW/cm^2]	nB [–]	nPD [–]
Al-BSF(5″)	132.5	3.5	0.51	0.55
Al-BSF(6″)	97.9	3.5	0.38	0.56
Al-BSF(BF)	91.4	3.5	0.35	0.55
IBC	180.6	2.5	0.69	0.40
PERC	103.0	2.9	0.39	0.46
SHJ	112.7	2.7	0.43	0.43
TOPCon	148.2	4.1	0.56	0.65

this solution reveals the optimal tradeoffs. A novel parameter, Energy-Communication Efficiency (EnCE), is introduced to identify the Pareto optimality. This parameter essentially is the product of normalized power density (nPD) and normalized bandwidth (nB), each calculated against the maximum power density (6.3 mW/cm^2) and bandwidth (261 kHz) recorded among all PV laminates. Fig. 20 shows the EnCE of the PV laminates, with their nPD denoted by the color bar and nB indicated by the size of the circles. Clearly, the tradeoff between energy harvesting and communication is evident, where lighter colors are accompanied by smaller circle sizes. Higher EnCEs are typically observed at moderate levels of nPD and nB. Among all the tested PV technologies, the TOPCon PV laminate outperforms by delivering the best EnCE, followed by the Al-BSF(5″) and IBC laminates with a comparable overall performance. This finding signifies that TOPCon offers the most balanced solution between the competing objectives

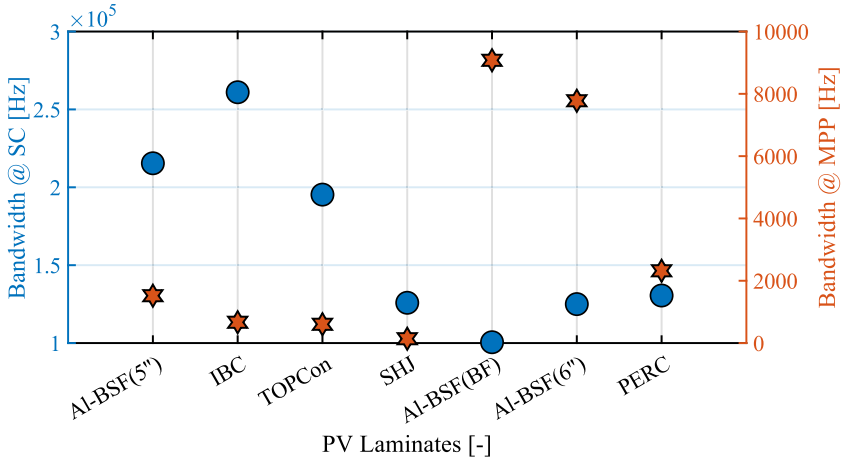

Fig. 15. Voltage bandwidth of PV laminates at short-circuit condition (blue circles) and maximum power point (red hexagrams) under blue LED at 300 W/m^2. The doping concentration of PV laminates increases from left to right, where Al-BSF(5″) has the lowest doping concentration and PERC has the highest.

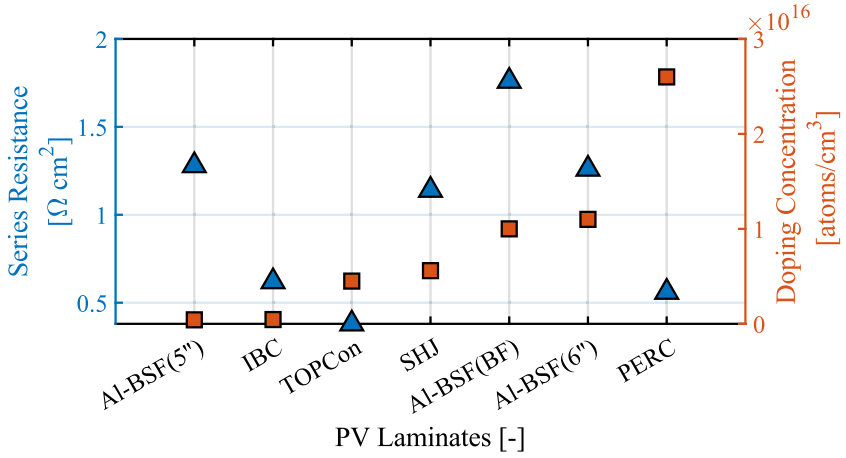

Fig. 16. Series resistance and doping concentration of PV laminates, where the series resistance is extracted from the I–V measurement under blue LED at 300 W/m^2. The doping concentration of PV laminates increases from left to right, where Al-BSF(5″) has the lowest doping concentration and PERC has the highest.

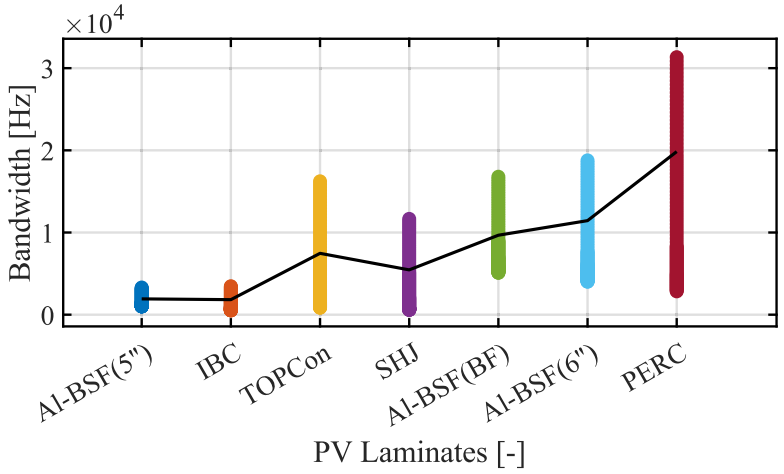

Fig. 17. Bandwidths of PV laminates with each color bar representing the bandwidths at operating voltages from 450 to 550 mV displayed from top to bottom. The bandwidths at 475 mV are connected by a black line, and it shows an ascending trend as the doping concentration increases from left to right, where Al-BSF(5″) has the lowest doping concentration and PERC has the highest.

within a PV-based VLC system, making it the most preferred choice among all available alternatives when the system is designed for Pareto optimality. The absolute power density and bandwidth for each PV laminate at the Pareto optimality are listed in Table 3.

5. Conclusions

In this work, the dynamic performance of seven commercial c-Si PV laminates used as receivers in the VLC link is investigated.

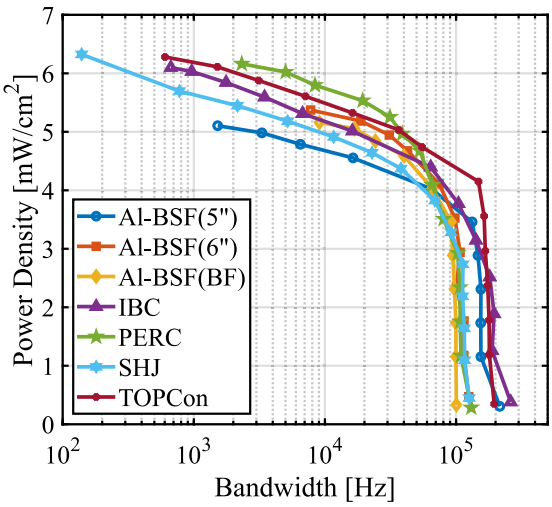

Fig. 18. Voltage bandwidths of PV laminates versus their power output under blue LED at 300 W/m^2.

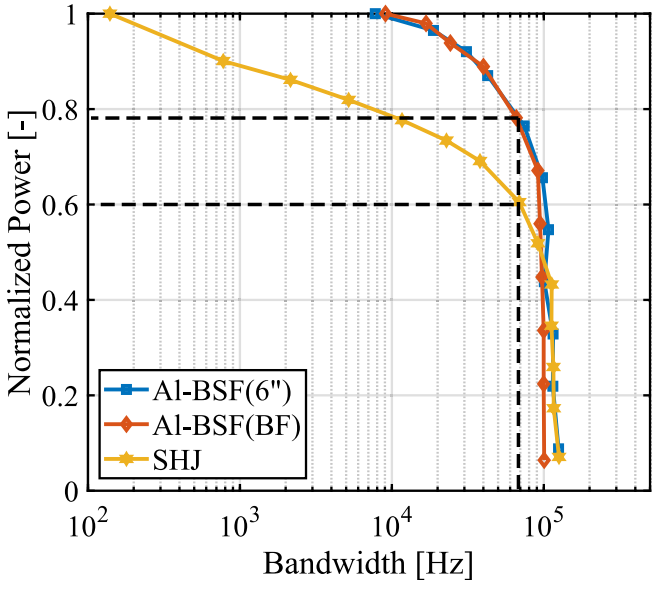

Fig. 19. Voltage bandwidths of Al-BSF(5″), Al-BSF(BF), and SHJ PV laminates versus their normalized power output under blue LED at 300 W/m^2. To achieve the same bandwidth, SHJ loses 40% of its output power, whereas the other two laminates can still deliver 80% of their maximum power.

These laminates include various architectures: Al-BSF(5″), Al-BSF(6″), Al-BSF(BF), IBC, PERC, SHJ, and TOPCon. The measurements are conducted under three LED colors (blue, green, and red) configured at three different irradiance levels (100, 300, and 500 W/m^2). For each lighting condition, the PV laminate is biased at various operating voltages spanning from short-circuit to open-circuit. At each operating voltage, the frequency sweep is performed by superimposing a small AC signal (ranging from 25 to 250 kHz) onto the constant DC signal of the LED light source to characterize the bandwidth of each PV laminate.

The measurement results indicate that the operating voltage of PV laminates significantly impacts their bandwidth. Increasing the operating voltage leads to decreased bandwidth, and two distinct variation ranges are identified. In the low operating voltage range, where the depletion capacitance is the controlling factor, the bandwidth decreases gradually with increasing voltage. Conversely, in the high operating voltage range, the bandwidth variation is primarily dominated by the diffusion capacitance, which changes exponentially with rising voltage. Given that the operating voltage also determines the output power of the PV laminate, it becomes apparent that achieving high bandwidth and maximizing power production are conflicting objectives. Therefore, a trade-off exists between energy harvesting and data transmission when PV cells are used as VLC receivers.

The second key observation reveals that the irradiance level also influences the bandwidth of PV laminates, where the dominant mechanism is the larger resistance R' of the PV laminate under low-light conditions. This effect is more noticeable in the low operating voltage range, where the impact of depletion capacitance on the bandwidth is relatively minor compared to the increased resistance under low-light conditions. However, at higher operating voltages, the bandwidth is predominantly determined by the diffusion capacitance, and the effect of increased resistance under low-light conditions becomes less significant. Therefore, higher irradiance levels are more beneficial for communication when the PV laminate is operating at lower voltages. In contrast, when the PV laminate is working at its maximum power point, the impact of irradiance level on the communication performance is minor. It is worth noting that in this study, the LED light source was used for both energy harvesting and communication. Future investigations into the impact of irradiance levels on communication performance in an outdoor environment could be conducted by using a system with individual light sources, where one only serves as the background light for energy production, and the other one is dedicated to communication. The LED color has a marginal influence on the bandwidth of PV laminates across the entire operating voltage range and irradiance levels. This consistent bandwidth performance is advantageous to the WDM integration with LEDs and simplifies the color filter design for signal separation and demodulation with multiple PV cells. Depending on the application-specific requirements, using blue LED is more energy-efficient, while choosing red LED enables relatively longer-distance communication.

Among the various tested PV laminates, Al-BSF(5″) and Al-BSF(BF) demonstrate the least bandwidth fluctuation as the output power increases to the MPP in a VLC system, while TOPCon PV laminate emerges as the best candidate when the system is designed for the Pareto optimality between energy harvesting and communication. The impact of the architecture of the commercial c-Si PV laminates can be mainly attributed to the bulk doping concentration and the metallization design. Optimizing the metallization design to reduce the resistance benefits both energy production and communication. Higher doping concentration increases the depletion capacitance, leading to a lower bandwidth when the PV laminates are biased at low operating voltages. However, at higher operating voltages, including those around MPP, the diffusion capacitance that decreases with increased doping concentration dictates, resulting in a higher bandwidth. Therefore, a higher bulk doping concentration is preferred as long as it does not adversely affect the conversion efficiency of PV cells, since they are expected to operate at MPP to maximize energy harvesting. Future studies could focus on the optimization of parameters of doping concentration and metallization design to enhance both energy harvesting and communication. At the module level, the individual impact of capacitance and resistance on the bandwidth due to the interconnection of cells should be balanced out, but the additional metallization and the junction box can introduce unwanted extra resistance, potentially degrading communication performance. Future studies could investigate the influence of module fabrication on bandwidth to address these potential issues. Moreover, PV modules under operation are often subject to non-uniform illumination such as partial shading, leading to cells working at different operating points. Future studies could investigate this intra-module non-uniformity on the bandwidth of PV modules and explore novel approaches to deal with this issue such as innovative design of module circuit.

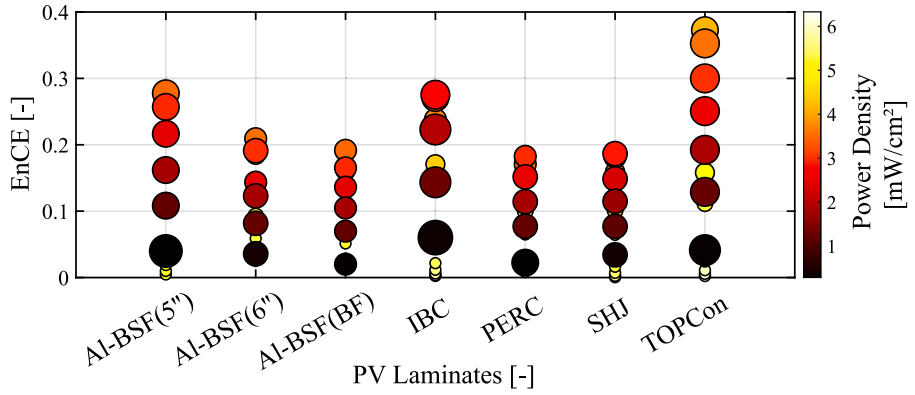

Fig. 20. The EnCE for tested PV laminates under blue LED at 300 W/m^2. The color bar denotes the scale of power density, and the size of the circle represents the scale of normalized bandwidth.

CRediT authorship contribution statement

Yilong Zhou: Writing – review & editing, Writing – original draft, Visualization, Methodology, Investigation, Formal analysis, Data curation, Conceptualization. **Aya Ibrahim:** Investigation, Formal analysis, Data curation. **Mirco Muttillo:** Writing – review & editing, Supervision, Software, Methodology, Investigation, Formal analysis, Data curation, Conceptualization. **Hesan Ziar:** Supervision, Methodology, Conceptualization. **Olindo Isabella:** Writing – review & editing, Supervision, Resources, Project administration, Funding acquisition. **Patrizio Manganiello:** Writing – review & editing, Supervision, Project administration, Methodology, Formal analysis, Conceptualization.

Declaration of competing interest

The authors declare that they have no known competing financial interests or personal relationships that could have appeared to influence the work reported in this paper.

Acknowledgments

This work was supported by the project Future Factory, The Netherlands (TEUE919002), which received funding from the Dutch Ministry of Economic Affairs and Climate Policy, The Netherlands. The authors would like to thank Stefaan Heirman for his contribution to the experimental setup and Rick van Dyck for his contribution to the characterization of PV laminates under STC.

Appendix. Determination of damping ratio condition and inductance

The equation for resonant frequency calculation is given in Eq. (9). At lower operating voltages, the capacitance of the PV laminate is primarily determined by the depletion capacitance, which is relatively small in magnitude compared to the diffusion capacitance encountered at higher operating voltages. Therefore, the inductance effect becomes more pronounced at these lower PV operating voltages, leading to an underdamped system. As the PV operating voltage increases, both the capacitance and load resistance of the PV laminate system increase, leading to a higher damping ratio given by Eq. (A.1):

$$\zeta = \frac{R'}{2}\sqrt{\frac{C}{L}} \tag{A.1}$$

Fig. A.21 exemplifies this behavior, showcasing the system with constant inductance ($L = 10$ nH) but subject to different resistance and capacitance. The blue curve depicts an underdamped system when the PV laminate is working at low voltages ($R' = 5$ mΩ, $C = 1$ μF), while the red curve shows the case of an overdamped system at elevated PV voltages ($R' = 20$ mΩ, $C = 100$ μF). With resistance and capacitance being

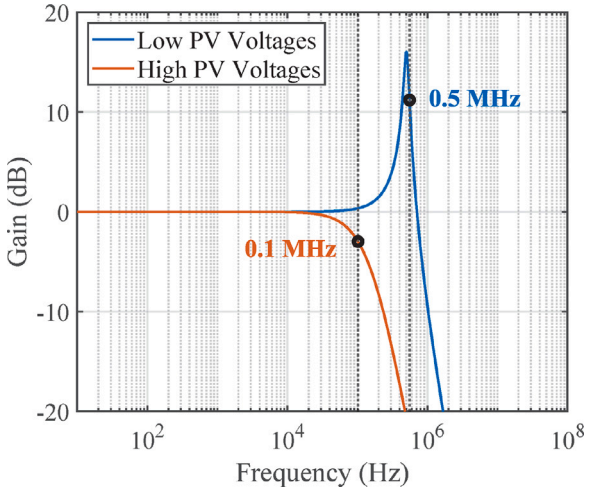

Fig. A.21. The logarithmically scaled frequency response of an equivalent RLC low-pass filter circuit, illustrating scenarios with low and high PV operating voltages. The responses are depicted by the blue curve (low PV voltage) and the red curve (high PV voltage), respectively. The increased resistance and capacitance at high PV voltages overdamped the system, and the frequency response of this system can be effectively modeled by an equivalent RC circuit.

the dominant components, the system transitions from underdamped ($\zeta < 1$) to overdamped ($\zeta > 1$) as the PV voltage increases, and the oscillatory response diminishes. Consequently, the frequency response closely resembles an RC low-pass filter, and the system bandwidth decreases from 0.5 MHz to 0.1 MHz. This phenomenon suggests that the RLC frequency response of the PV laminate, particularly under high operating voltages, can be effectively approximated by an equivalent RC circuit, and its bandwidth can be readily determined using Eq. (5).

The correction after considering the inductance-induced resonance is mainly performed by comparing the bandwidths derived from equations for the cut-off frequency and for the resonant frequency, where the lower of these two values is selected as the true bandwidth of the PV laminate:

$$\frac{1}{2\pi\sqrt{LC}} < \frac{1}{2\pi R'C} \tag{A.2}$$

This condition can be further refined and becomes:

$$R' < \sqrt{\frac{L}{C}} \tag{A.3}$$

where the capacitance C is obtained from Eqs. (2) and (3), and the resistance R' is calculated from Eq. (6). By incorporating Eq. (A.1), the

condition can be exclusively expressed in terms of the damping ratio:

$$\zeta < \frac{1}{2} \tag{A.4}$$

To determine the inductance L, the PV laminate is first short-circuited with a wire on which the voltage drop V_{wire} is measured. The frequency sweep is then performed, and the resonant frequency f_{short} is extracted. After that, the PV laminate is disconnected from the wire and reconnected to the bias driver, which is adjusted to replicate the same voltage drop V_{wire} across the PV laminate. A second frequency sweep is then performed to extract the cut-off frequency, which is used to obtain the capacitance C_{short}. Assuming a constant capacitance and inductance across both measurements, the inductance can be derived by:

$$L = \frac{1}{4\pi^2 f_{short}^2 C_{short}} \tag{A.5}$$

Data availability

Data will be made available on request.

References

[1] IoT connected devices worldwide 2019–2030 | Statista, [Online]. Available: https://www.statista.com/statistics/1183457/iot-connected-devices-worldwide/.

[2] Schieler CM, Riesing KM, Bilyeu BC, Chang JS, Garg AS, Gilbert NC, Horvath AJ, Reeve RS, Robinson BS, Wang JP, Piazzolla S, Roberts WT, Kovalik JM, Keer B. On-orbit demonstration of 200-gbps laser communication downlink from the TBIRD CubeSat. In: Free-space laser communications XXXV. SPIE; 2023, 1241302.

[3] Satellite Communication | TNO, [Online]. Available: https://www.tno.nl/en/sustainable/space-scientific-instrumentation/satellite-communication/laser-satellite-communication/.

[4] Haas H, Sarbazi E, Marshoud H, Fakidis J. Visible-light communications and light fidelity. Opt Fiber Telecommun VII 2020;443–93.

[5] Feng L, Hu RQ, Wang J, Xu P, Qian Y. Applying VLC in 5G networks: Architectures and key technologies. IEEE Netw 2016;30(6):77–83.

[6] Claussen H, Ho LT, Samuel LG. An overview of the femtocell concept. Bell Labs Tech J 2008;13(1):221–45.

[7] Islim MS, Xie E, Haas H, Dawson MD, Viola S, Ferreira RX, Bamiedakis N, He X, Watson S, Penty RV, Kelly AE, Videv S, White IH, Gu E. Towards 10Gb/s orthogonal frequency division multiplexing-based visible light communication using a GaN violet micro-LED. Photonics Res 2017;5(2):A35–43.

[8] Elgala H, Mesleh R, Haas H. Indoor optical wireless communication: Potential and state-of-the-art. IEEE Commun Mag 2011;49(9):56–62.

[9] Wang Z, Tsonev D, Videv S, Haas H. On the design of a solar-panel receiver for optical wireless communications with simultaneous energy harvesting. IEEE J Sel Areas Commun 2015;33(8):1612–23.

[10] Haas H, Yin L, Wang Y, Chen C. What is lifi? J Lightwave Technol 2016;34(6):1533–44.

[11] Jovicic A, Li J, Richardson T. Visible light communication: opportunities, challenges and the path to market. IEEE Commun Mag 2013;51(12):26–32.

[12] Wu JT, Chow CW, Liu Y, Hsu CW, Yeh CH. Performance enhancement technique of visible light communications using passive photovoltaic cell. Opt Commun 2017;392:119–22.

[13] Wi-Fi Boosts New, Ultrafast Li-Fi Standards - IEEE Spectrum, [Online]. Available: https://spectrum.ieee.org/lifi-standards.

[14] Hossain MM, Ray S, Cheong JS, Qiao L, Baharuddin AN, Hella MM, David JP, Hayat MM. Low-noise speed-Optimized Large Area CMOS avalanche photodetector for visible light communication. J Lightwave Technol 2017;35(11):2315–24.

[15] Lorriere N, Betrancourt N, Pasquinelli M, Chabriel G, Barrere J, Escoubas L, Wu JL, Bermudez V, Ruiz CM, Simon JJ. Photovoltaic solar cells for outdoor lifi communications. J Lightwave Technol 2020;38(15):3822–31.

[16] Chen X, Min C, Guo J. Visible light communication system using silicon photocell for energy gathering and data receiving. Int J Opt 2017;2017.

[17] Kim SM, Won JS. Simultaneous reception of visible light communication and optical energy using a solar cell receiver. Int Conf ICT Convergence 2013;896–7.

[18] Malik B, Zhang X. Solar panel receiver system implementation for visible light communication. Proc IEEE Int Conf Electron Circuits Syst 2016;502–3.

[19] Wang Z, Tsonev D, Videv S, Haas H. Towards self-powered solar panel receiver for optical wireless communication. IEEE Int Conf Commun 2014;3348–53.

[20] Shin W-H, Yang S-H, Kwon D-H, Han S-K. Self-reverse-biased solar panel optical receiver for simultaneous visible light communication and energy harvesting. Opt Express 2016;24(22):A1300–5.

[21] Kong M, Sun B, Sarwar R, Shen J, Chen Y, Qu F, Han J, Chen J, Qin H, Xu J. Underwater wireless optical communication using a lens-free solar panel receiver. Opt Commun 2018;426:94–8.

[22] Das S, Poves E, Fakidis J, Sparks A, Videv S, Haas H. Towards energy neutral wireless communications: Photovoltaic cells to Connect Remote Areas. Energies 2019;12(19):3772.

[23] Das S, Sparks A, Poves E, Videv S, Fakidis J, Haas H. Effect of sunlight on photovoltaics as optical wireless communication receivers. J Lightwave Technol 2021;39(19):6182–90.

[24] Kong M, Lin J, Kang CH, Shen C, Guo Y, Sun X, Sait M, Weng Y, Zhang H, Ng TK, Ooi BS. Toward self-powered and reliable visible light communication using amorphous silicon thin-film solar cells. Opt Express 2019;27(24):34542–51.

[25] Manousiadis PP, Yoshida K, Turnbull GA, Samuel ID. Organic semiconductors for visible light communications. Phil Trans R Soc A 2020;378(2169).

[26] Arredondo B, Romero B, Sánchez Pena JM, Fernández-Pacheco A, Alonso E, Vergaz R, de Dios C. Visible light communication system using an organic bulk heterojunction photodetector. Sensors 2013;13(9):12266–76.

[27] Vega-Colado C, Arredondo B, Torres JC, López-Fraguas E, Vergaz R, Martín-Martín D, Del Pozo G, Romero B, Apilo P, Quintana X, Geday MA, de Dios C, Sánchez-Pena JM. An all-organic flexible visible light communication system. Sensors 2018;18(9):3045.

[28] Salamandra L, La Notte L, Fazolo C, Di Natali M, Penna S, Mattiello L, Cinà L, Del Duca R, Reale A. A comparative study of organic photodetectors based on P3HT and PTB7 polymers for visible light communication. Organ Electron 2020;81:105666.

[29] Zhang S, Tsonev D, Videv S, Ghosh S, Turnbull GA, Samuel IDW, Haas H. Organic solar cells as high-speed data detectors for visible light communication. Optica 2015;2(7):607–10.

[30] Tavakkolnia I, Jagadamma LK, Bian R, Manousiadis PP, Videv S, Turnbull GA, Samuel ID, Haas H. Organic photovoltaics for simultaneous energy harvesting and high-speed MIMO optical wireless communications. Light Sci Appl 2021;10(1).

[31] Mica NA, Bian R, Manousiadis P, Jagadamma LK, Tavakkolnia I, Haas H, Haas H, Turnbull GA, Turnbull GA, Samuel IDW, Samuel IDW. Triple-cation perovskite solar cells for visible light communications. Photonics Res 2020;8(8):A16–24.

[32] Fakidis J, Videv S, Helmers H, Haas H. 0.5-Gb/s OFDM-based laser data and power transfer using a GaAs photovoltaic cell. IEEE Photonics Technol Lett 2018;30(9):841–4.

[33] Fakidis J, Helmers H, Haas H. Simultaneous wireless data and power transfer for a 1-Gb/s GaAs VCSEL and photovoltaic link. IEEE Photonics Technol Lett 2020;32(19):1277–80.

[34] Monokroussos C, Gottschalg R, Tiwari AN, Friesen G, Chianese D, Mau S. The effects of solar cell capacitance on calibration accuracy when using a flash simulator. In: IEEE 4th world conference on photovoltaic energy conference. vol. 2, 2006, p. 2231–4.

[35] Braun S, Micard G, Hahn G. Solar cell improvement by using a multi busbar design as front electrode. Energy Procedia 2012;27:227–33.

[36] Chen N, Tune D, Buchholz F, Roescu R, Zeman M, Isabella O, Mihailetchi VD. Stable passivation of cut edges in encapsulated n-type silicon solar cells using nafion polymer. Sol Energy Mater Sol Cells 2023;258:112401.

[37] SR-1901PT - Spectral Evolution, [Online]. Available: https://spectralevolution.com/product/sr-1901pt/.

[38] van Nijen DA, Muttillo M, Van Dyck R, Poortmans J, Zeman M, Isabella O, Manganiello P. Revealing capacitive and inductive effects in modern industrial c-Si photovoltaic cells through impedance spectroscopy. Sol Energy Mater Sol Cells 2023;260:112486.

[39] LOANA solar cell analysis system, [Online]. Available: http://www.pv-tools.de/products/loana-system/loana-start.html.

[40] Smets AHM, Jäger K, Isabella O, Swaaij RAv, Zeman M. Solar energy: The physics and engineering of photovoltaic conversion, technologies and systems. UIT Cambridge Limited; 2016, p. 119–21.

[41] Kong M, Kang CH, Alkhazragi O, Sun X, Guo Y, Sait M, Holguin-Lerma JA, Ng TK, Ooi BS. Survey of energy-autonomous solar cell receivers for satellite–air–ground–ocean optical wireless communication. Prog Quantum Electron 2020;74:100300.

[42] Thermal Effects on White LED Chromaticity | DigiKey, [Online]. Available: https://www.digikey.com/en/articles/thermal-effects-on-white-led-chromaticity.

[43] Pravettoni M, Poh D, Prakash Singh J, Wei Ho J, Nakayashiki K. The effect of capacitance on high-efficiency photovoltaic modules: A review of testing methods and related uncertainties. J Phys D: Appl Phys 2021;54(19).

[44] Edler A, Schlemmer M, Ranzmeyer J, Harney R. Understanding and overcoming the influence of capacitance effects on the measurement of high efficiency silicon solar cells. Energy Procedia 2012;27:267–72.

[45] Yaqoob SJ, Saleh AL, Motahhir S, Agyekum EB, Nayyar A, Qureshi B. Comparative study with practical validation of photovoltaic monocrystalline module for single and double diode models. Sci Rep 2021;11(1):1–14.

[46] Thongpron J, Kirtikara K, Jivacate C. A method for the determination of dynamic resistance of photovoltaic modules under illumination. Sol Energy Mater Sol Cells 2006;90(18–19):3078–84.

[47] Sindhubala K, Vijayalakshmi B. Receiver intend to reduce ambient light noise in visible-light communication using solar panels. J Eng Sci Technol Rev 2017;10(1):84–90.
[48] Bunea GE, Wilson KE, Meydbray Y, Campbell MP, De Ceuster DM. Low light performance of mono-crystalline silicon solar cells. In: Conference record of the 2006 IEEE 4th world conference on photovoltaic energy conversion. WCPEC-4, vol. 2, IEEE Computer Society; 2006, p. 1312–4.
[49] Kim T-K. Visible light communication using RGB LED for machine-to-machine communication. Int J Mech Eng Technol 2019;9(13):951–8.
[50] Kusuma P, Pattison PM, Bugbee B. From physics to fixtures to food: current and potential LED efficacy. Hortic Res 2020;7(1):1–9.
[51] Rayleigh Scattering - an overview | ScienceDirect Topics, [Online]. Available: https://www.sciencedirect.com/topics/physics-and-astronomy/rayleigh-scattering.
[52] Pareto Optimality - an overview | ScienceDirect Topics, [Online]. Available: https://www.sciencedirect.com/topics/engineering/pareto-optimality.